nature photonics

REVIEW ARTICLE

https://doi.org/10.1038/s41566-020-00741-3

Extreme-ultraviolet frequency combs for precision metrology and attosecond science

Ioachim Pupeza[1,2] ✉, Chuankun Zhang[3,4], Maximilian Högner[1] and Jun Ye[3,4] ✉

Femtosecond mode-locked lasers producing visible/infrared frequency combs have steadily advanced our understanding of fundamental processes in nature. For example, optical clocks employ frequency-comb techniques for the most precise measurements of time, permitting the search for minuscule drifts of natural constants. Furthermore, the generation of extreme-ultraviolet attosecond bursts synchronized to the electric field of visible/infrared femtosecond pulses affords real-time measurements of electron dynamics in matter. Cavity-enhanced high-order harmonic generation sources uniquely combine broadband vacuum- and extreme-ultraviolet spectral coverage with multimegahertz pulse repetition rates and coherence properties akin to those of frequency combs. Here we review the coming of age of this technology and its recent applications and prospects, including precision frequency-comb spectroscopy of electronic and potentially nuclear transitions, and low-space-charge attosecond-temporal-resolution photoelectron spectroscopy with nearly 100% temporal detection duty cycle.

The control over broadband visible/near-infrared (VIS/NIR) electromagnetic waves, such as uniquely enabled by laser architectures employing mode-locked oscillators, lies at the heart of most advanced optical metrologies. The temporal interplay between gain, loss, dispersion and nonlinear propagation in a mode-locked oscillator[1] results in a train of equidistant output pulses with highly reproducible pulse-to-pulse intensity envelopes, and with durations as short as just several femtoseconds—orders of magnitude shorter than the characteristic times of modern electronics. This outstanding temporal confinement of optical intensity has, for example, enabled time-resolved studies of molecular dynamics, establishing the field of femtochemistry[2].

The additional control of the phase of the optical carrier wave with respect to its intensity envelope[3–6] brought about the next—and so far highest—level of temporal resolution in optical experiments. The amplification, nonlinear spectral broadening and subsequent temporal compression of phase-coherent femtosecond light pulses (reviewed in ref. [7]) led to the generation of reproducible optical waveforms comprising merely a few oscillations of the VIS/NIR carrier electric field, which can be focused to reach peak field strengths exceeding the binding Coulomb fields of atoms. The extremely fast rise of the oscillating optical electric field to such high strengths allows for strong-field-induced ionization[8] and recollision dynamics in gas atoms, underlying coherent high-order harmonic generation (HHG)[9–11]. The HHG process itself, and the emerging high-photon-energy attosecond bursts[12], represented the fastest controlled dynamics, and the shortest generated events, respectively. This marked the birth of attosecond metrology[13] around the last turn of the century, opening the door to the study of electron motion in atoms[14–16], molecules[17,18], condensed matter[19–23] and nanostructures[24–26].

In the frequency domain, the train of temporally equidistant pulses output by a (phase stabilized) mode-locked laser exhibits a spectral structure consisting of a multitude of equidistant narrow lines, forming an optical frequency comb[27,28]. The optical (angular) frequency ω_N of each such 'comb mode' can be parameterized as $\omega_N = \omega_0 + N\omega_r$. Here $\omega_r = 2\pi/T_r$ and ω_0 are two frequencies in the radiofrequency domain, corresponding to the inverse round-trip time T_r of the optical pulse inside the mode-locked oscillator and to an overall comb-offset frequency, respectively, and N is an integer. With N on the order of ~10^6, precise control of the two degrees of freedom for the comb provides a convenient, robust and phase-coherent link between the optical frequency domain of ω_N, lying in the few to hundreds of terahertz range, and the radiofrequency domain (~100 MHz). This affords a unique, high-precision means of measuring and comparing optical frequencies. Nowadays, frequency-comb technology is employed as the clockwork in modern optical atomic clocks, potentially permitting a more precise definition of the second based on optical standards[29,30]. At the same time, frequency combs have emerged as a powerful tool for spectroscopy that simultaneously achieves broad spectral coverage and high spectral resolution[31–33].

The availability of broadband, table-top radiation sources, spectrally covering the vacuum-ultraviolet, extreme-ultraviolet and soft X-ray ranges (henceforth abbreviated as 'XUV'), and exhibiting optical phase coherence and high repetition rates akin to frequency combs, promises a substantial impact on precision frequency metrology, photoelectron spectroscopy (PES) and attosecond science. In the absence of broadband laser gain media and optics suitable for building mode-locked oscillators in the XUV range, frequency upconversion of the pulse train emitted by a VIS/NIR mode-locked laser via HHG represents the only viable route. To this end, the individual VIS/NIR pulses, sequenced at a high repetition rate, need to reach the high peak intensities necessary for HHG. In turn, the precise control now mastered for VIS/NIR frequency combs can be transferred via HHG to achieve high phase coherence in the XUV domain[34–36].

Among table-top coherent XUV radiation sources (Fig. 1), femtosecond enhancement cavities (fsECs)[37,38] provide VIS/NIR pulses driving HHG with a unique combination of high peak intensities with high repetition rates. In an fsEC, the unconverted portion of the energy of the VIS/NIR pulses is recycled after each

[1]Max-Planck-Institut für Quantenoptik, Garching, Germany. [2]Ludwig-Maximilians-Universität München, Munich, Germany. [3]JILA, National Institute of Standards and Technology and University of Colorado, Boulder, CO, USA. [4]Department of Physics, University of Colorado, Boulder, CO, USA. ✉e-mail: ioachim.pupeza@mpq.mpg.de; ye@jila.colorado.edu

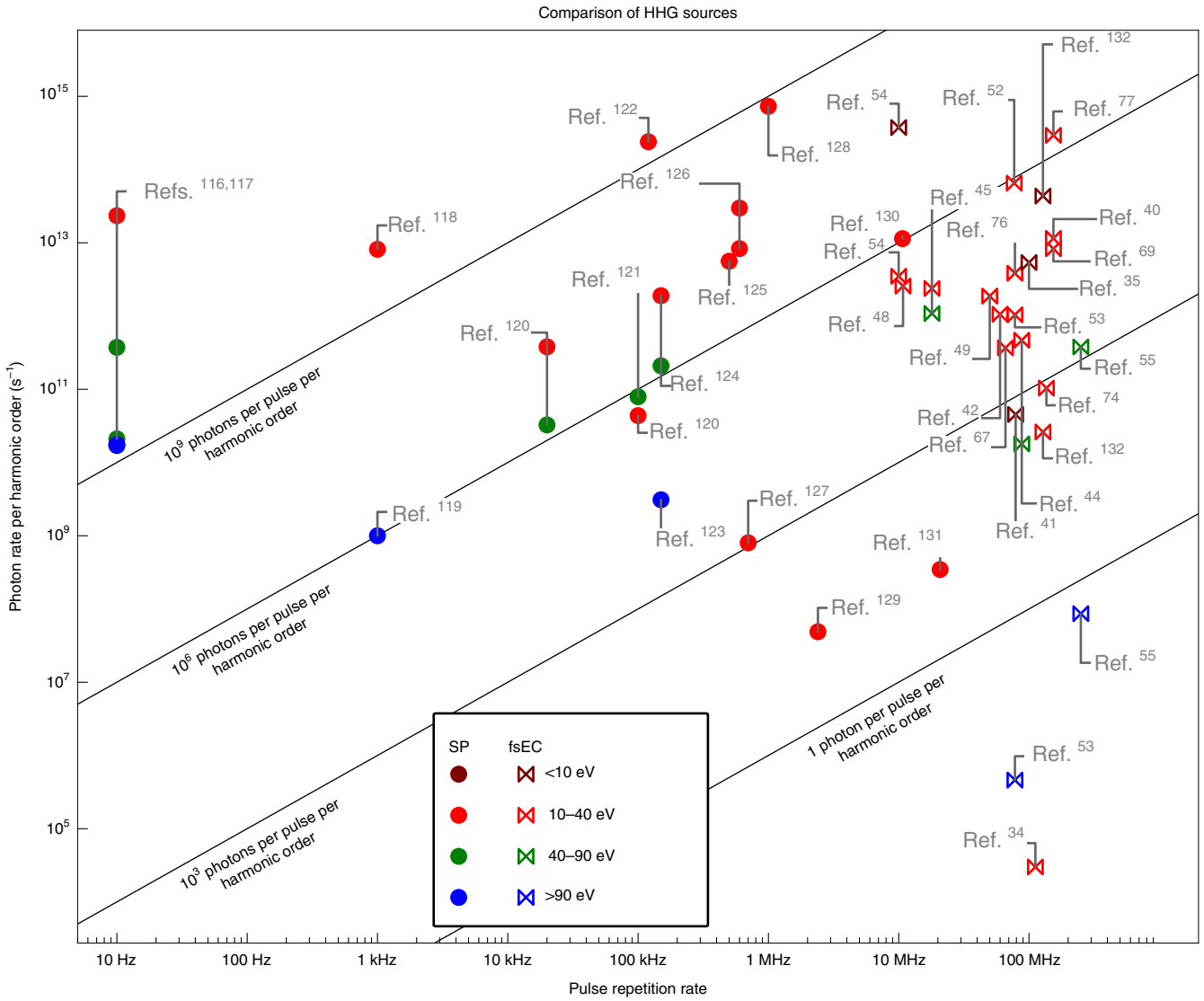

Fig. 1 | Representative selection of state-of-the-art HHG sources. The photon rate (available for experiments) is plotted as a function of the repetition rate of the HHG driving pulses. The colour coding illustrates different wavelength ranges. For each range, the photon rate of the strongest harmonic is shown. The circle and the bowtie symbols indicate single-pass (SP) and fsEC-based HHG sources, respectively. Cavity-enhanced sources uniquely afford HHG at repetition rates of several tens of megahertz, with photon rates of up to 10^6 photons per pulse, and photon energies of several tens of electronvolts. Data from refs. [115–132].

interaction with the HHG medium (typically a gas target). This uniquely affords high peak intensities necessary for efficient HHG despite the moderate energy of the individual pulses available from multimegahertz-repetition-rate lasers. Since their first demonstration[34,35] in 2005, concentrated development efforts have advanced these coherent XUV sources to a maturity that renders them suitable for time- and for frequency-domain precision metrology, as well as for PES of condensed matter combining high energy resolution with high photon energies. In this Review, we survey the milestones of these developments, emphasizing the progress since the last comprehensive review on the topic[39]. We then summarize recent applications of fsEC-based HHG sources to precision measurements of quantum transitions[40,41] and to low-space-charge PES of solids[42–45]. We conclude with an outlook on experiments that promise a particularly high impact on science and technology in the near future, namely the construction of nuclear-based optical clocks and multidimensional attosecond PES of solids.

Resonant enhancement of femtosecond pulses

The mode of operation of an fsEC is illustrated in Fig. 2. The multimegahertz-repetition-rate VIS/NIR pulse train emitted by a (phase stabilized) mode-locked-oscillator-based laser system (Fig. 2a) is coupled to a free-space, passive optical resonator[37], the fsEC, by means of a partially transmitting input coupling mirror. The resonator normally fulfils the stability criterion[46], ensuring low-diffraction-loss propagation of a coherent light beam within well-defined transverse eigenmodes. Efficient coupling of the seeding pulse train to the passive resonator necessitates constructive interference of the electric field of each input pulse with the circulating pulse. Typically, a ring (that is, travelling wave) resonator is employed to ensure unidirectional output of the intracavity-generated radiation.

The input pulse train and the corresponding frequency comb are illustrated in Fig. 2a,b, respectively. The resonance condition for optimum power enhancement requires that both the repetition

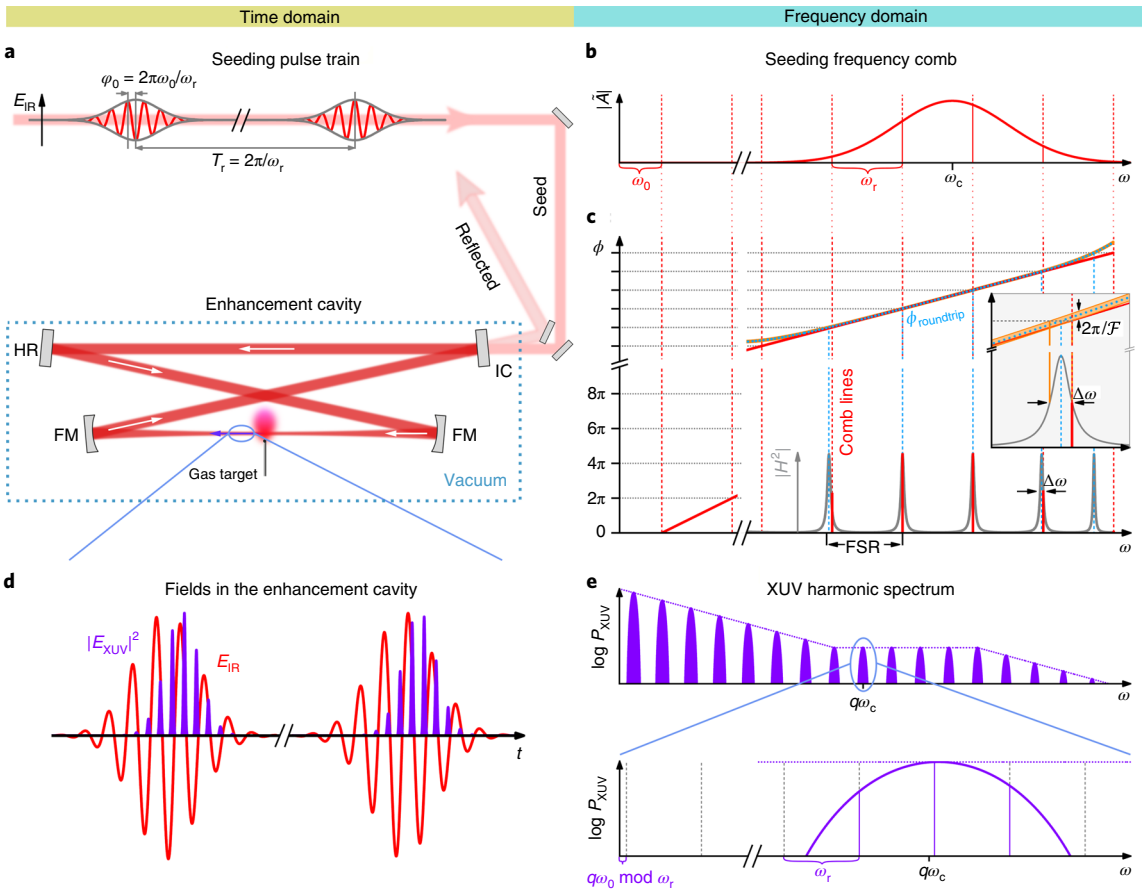

Fig. 2 | Mode of operation of cavity-enhanced HHG. a, A train of (infrared) pulses with the electric field E_{IR}, a repetition period $T_r = 2\pi/\omega_r$ and a pulse-to-pulse carrier-envelope offset slippage $\varphi_0 = 2\pi\omega_0/\omega_r$, where ω_0 and ω_r are the frequency-comb parameters (see text), is coupled to a passive resonator containing a gas target at a focus. IC, partially transmitting input coupling mirror; HR, highly reflective mirror; FM, focusing HR. The choice of small angles of incidence on the resonator mirrors (as typical for dielectric optics) together with beam folding aiming at a compact footprint, typically result in a bowtie geometry. **b**,**c**, Frequency-domain representation of the spectra $|\tilde{A}|$ of the input pulse train, centred at ω_c (**b**) and of the resonator transfer function (**c**), the latter assuming a linear cavity response. Unlike the frequency-comb modes, the cavity resonances are not equidistant in the frequency domain, which is a consequence of residual dispersion of the round-trip phase $\phi_{roundtrip}(\omega)$ (dotted blue line, referring to the vertical axis for phase ϕ). The power enhancement $|H|^2$ drops to half its peak value[58] if the round-trip phase $\phi_{roundtrip}(\omega)$ deviates from a linear phase by $\pi/\mathcal{F}(\omega)$ (orange corridor, see also inset with zoom on second-from-right resonance). **d**, Illustration of XUV pulse train (represented by the squared magnitude of its temporal envelope, $|E_{XUV}|^2$) emerging via HHG in the gas target: each half-cycle of the driving field emits an XUV pulse, rigidly locked to, and lagging the former by the electron excursion time, and whose intensity depends on the field amplitude. The horizontal axis represents time t. **e**, Generated XUV spectrum P_{XUV} (top), consisting of individual harmonics—which emerge via spectral interference of the XUV pulses within the attosecond pulse train (see panel **d**)—and the substructure of a harmonic (bottom), consisting of an XUV frequency comb with the original repetition frequency ω_r and an offset frequency equal to $q\omega_0$ modulo ω_r, where q denotes the (odd) harmonic order.

period and the pulse-to-pulse phase slippage of the optical carrier wave underneath the field envelope travelling in the fsEC be matched to the corresponding parameters of the input pulse train, that is, $T_r = 2\pi/\omega_r$ and $\varphi_0 = 2\pi\omega_0/\omega_r$, respectively[37]. In the frequency domain, this condition is equivalent to optimizing the overlap of the input frequency comb (parameterized by ω_0 and ω_r) with the resonance spectrum of the fsEC. Assuming a linear response of the resonator to the excitation, the latter is given by the transfer function $H(\omega)$, which for an input coupler with reflectivity $R(\omega)$ and transmission $T(\omega)$, for a round-trip attenuation $A(\omega)$ and a round-trip phase $\phi_{roundtrip}(\omega)$ reads[37,46]:

$$H(\omega) = \frac{\sqrt{T(\omega)}}{1 - \sqrt{R(\omega)A(\omega)}e^{i\phi_{roundtrip}(\omega)}}. \quad (1)$$

The frequency-dependent power enhancement $|H(\omega)|^2$ exhibits a comb-like structure of sharp resonances (Fig. 2c). In contrast to the spectrum of the seeding frequency comb (Fig. 2b), the resonances of a linear fsEC are in general not equidistant due to residual chromatic dispersion[47] (Fig. 2c). This brings about a spectral filtering effect, limiting the bandwidth that can be enhanced at once and, therefore, the pulse duration achievable in the linear-response fsEC. This effect increases for narrower resonances, that is, for higher resonator finesse $\mathcal{F}(\omega) \approx 2\pi/[1 - R(\omega)A(\omega)]$ (Fig. 2c).

The first fsEC for HHG were seeded by titanium:sapphire (Ti:Sa) oscillators[34,35,48], emitting spectra centred at approximately 800 nm. The average powers typical to these systems, on the order of 1 W, required high-finesse cavities to provide intracavity focal regions with peak intensities of 10^{13} W cm^{-2} or more, as necessary for HHG. With (spectrally averaged) finesse values of up to 2,000, these fsECs[39] supported circulating average powers between a few tens[34] and a few hundred[35,48] watts.

The short pulse durations typical to Ti:Sa oscillators, together with the aforementioned spectral filtering (particularly pronounced

at high finesse) led to a roughly 1.5-fold temporal elongation of the circulating pulses with respect to the seeding pulses, with the shortest reported circulating pulse duration of 28 fs (ref. [34]). A Ti:Sa-based laser system employing an injection-locked femtosecond amplification cavity provided seeding pulses with higher average power (6 W) and narrower spectrum (supporting 80 fs duration), which resulted in 1-kW-level circulating pulses without temporal elongation[49].

Shortly after the demonstration of the first Ti:Sa-based fsEC-HHG systems, the advent of high-power ytterbium (Yb)-based master-oscillator-power-amplifier lasers[50,51] afforded seeding pulse trains with average powers on the order of 100 W and pulse durations in the 100 to 250 fs range, spectrally centred around 1,030 nm. With these seeding lasers, multikilowatt-range intracavity average powers became a matter of course[36,40,42,44,45,52–54]—at moderate resonator finesse. Decreasing the finesse brings about a number of practical advantages for HHG, such as an increased spectral bandwidth and a reduced sensitivity to nonlinear effects (see next section). The pulse repetition rates of fsEC-HHG systems reported so far range from 10 MHz (refs. [48,54]) to 250 MHz (ref. [55]). Lower repetition rates are impeded by large resonator lengths. At high repetition rates, the efficiency of HHG suffers from cumulative plasma effects (see next section).

Some of the performance limits associated with fsECs can be tested in the absence of a nonlinear medium. The highest average powers reported so far for an empty fsEC are 670 kW and 400 kW for a 250 MHz train of 10 ps and 250 fs pulses, respectively[56], employing resonator designs with large illumination spots on all optics[57]. Nonlinear spectral broadening and dispersive temporal compression provides a convenient means of decreasing the pulse duration of high-power Yb-based lasers to the few 10 fs regime[53]. In an empty fsEC, for 30 fs pulses, 20 kW of average power has been demonstrated[55] and the shortest pulse reported in a kilowatt-level fsEC had a Fourier-transform limit of 17.5 fs, corresponding to 5 oscillation cycles of the carrier electric field[58]. Proper mirror and cavity design[56] reduces thermally induced distortions of the transverse mode to a negligible level for a typical fsEC operating at 10 kW average power level.

The importance of precisely controlling the round-trip phase triggered the development of cavity-comb locking[59] and several sensitive spectral-phase measurement techniques[47,58,60–63]. Furthermore, while the round-trip period of a pulse circulating in the fsEC can in good approximation be adjusted via the physical cavity length, for a given spectral coverage of the input comb, there is a well-defined value for ω_0 that maximizes the power enhancement[37,59]. This is due to a number of processes that affect the carrier-envelope phase of the pulse on propagation along the optic axis of the fsEC, including reflections from multilayer mirrors, Gouy phase shifts or transmission through dispersive elements/media along the beam path. In Fig. 2c, the optimum comb-offset frequency ω_0 is the intercept of the linear fit to the round-trip phase (red line) with the abscissa. For most applications, ω_0 of the seeding comb can be adjusted to optimize broadband enhancement. However, particular applications, such as the enhancement of waveform-stable pulses (that is, $\omega_0 = 0$) for the generation of isolated attosecond pulses via intracavity gating mechanisms[64], require careful control of the optimum offset frequency. Apart from (slight) tuning by intracavity dispersion or Gouy phase shifts, it has been shown that this can be achieved by means of dispersion-engineered multilayer mirrors[65].

Plasma dynamics and conversion efficiency

For cavity-enhanced HHG in gases, the ionizing medium must be placed in a high-intensity (focal) region of the resonator. This causes nonlinear effects at the wavelengths of the driving pulses, leading to a considerable deviation from the linear-fsEC response discussed in the previous section. As a general rule, this deviation increases with cavity finesse. For finesse values in the range of several hundred to a few thousand, power enhancement factors of 35 to 500 are routinely reached nowadays in the presence of intracavity high-pressure gas targets[44,45,52,53,66,67].

Active control of the interference of the intracavity circulating pulse with the seeding frequency comb (discussed later in the section 'XUV frequency-comb stability and coherence') enables the formation of an intracavity frequency comb with nominally the same comb parameters ω_0 and ω_r—despite the nonlinear distortions. HHG in the focal region produces a train of XUV attosecond pulses (one per half-cycle), rigidly locked to the electric field of the driving pulse[11] (Fig. 2d). The spectrum of the generated XUV radiation consists of high harmonics of the driving spectrum, of odd order[11] (Fig. 2e, top) and extending over several tens of electronvolts. The substructure of each harmonic (Fig. 2e, bottom) is that of a frequency comb with a repetition frequency equal to that of the original comb, and an offset frequency equal to $q\omega_0$ (modulo ω_r), where q denotes the harmonic order[34,35]. The produced XUV power equals the circulating power of the driving pulses times the conversion efficiency in the medium.

At the high repetition rates afforded by fsECs, each atom of the gas target is typically hit by multiple pulses before leaving the HHG volume (Fig. 3a). This leads to the formation of a cumulative plasma in (a part of) the interaction volume, impairing phase matching and, thus, considerably reducing the conversion efficiency compared with single-pass experiments, as well as complicating active stabilization (Fig. 3b)[68,69]. Operating at comparatively low repetition rates combined with tight focusing[45], and gas acceleration via heating or using mixtures with lower average molecular weight[52,55], reduce/circumvent the cumulative plasma effects and allow for conversion efficiencies in the gas target comparable to those of single-pass experiments, for repetition rates up to several tens of megahertz.

Even in the absence of cumulative effects, single-pulse self-induced spatiotemporal pulse distortions (Fig. 3c,d) impede recycling the driving pulses and limit the enhancement. Plasma-induced spectral blueshift and, at higher intensities, spatial distortions, lead to the phenomenon of intensity clamping[40,53,63,69,70] (Fig. 3e). Quantitative modelling allows for the choice of experimental parameters that mitigate this effect to an optimum[63], at which the amount of ionization in the gas target is limited. Intensity clamping can hinder driving HHG at optimum conversion efficiency. Nevertheless, recent experiments show that the conversion efficiency in the nonlinear medium can approach those of single-pass experiments at a power enhancement of around two orders of magnitude[45,52].

So far, cavity-enhanced HHG has only been demonstrated with the 'standard approach' of minimizing dispersion and losses of the linear cavity over a large bandwidth, and treating the nonlinearity as a disturbance in the operation of the linear fsEC. However, it is known that even with a strong nonlinearity that couples power to other wavelengths, low-loss steady states of the resonator such as dissipative cavity solitons exist[71,72]. For a gas nonlinearity, it has been suggested and theoretically shown that spectrally tailoring the cavity mirrors can give rise to such steady states, allowing for higher enhancement and considerably reduced intensity clamping[63]. Such new operating regimes for fsECs, possibly in conjunction with redshifting nonlinearities (using, for example, the Raman effect or optical parametric amplification) could provide routes towards considerably improved XUV power, with interesting properties such as noise filtering, intracavity pulse self-compression and broader bandwidths.

XUV output coupling

Even though the conversion efficiencies in the nonlinear medium in state-of-the-art fsEC-HHG setups approach those of single-pass experiments[45,52], efficiently coupling out the XUV radiation without obstructing cavity operation has been a major challenge[66,73]. The first systems employed a thin plate, transparent in the VIS/NIR, and placed under Brewster's angle after the HHG focus. Via reflection at

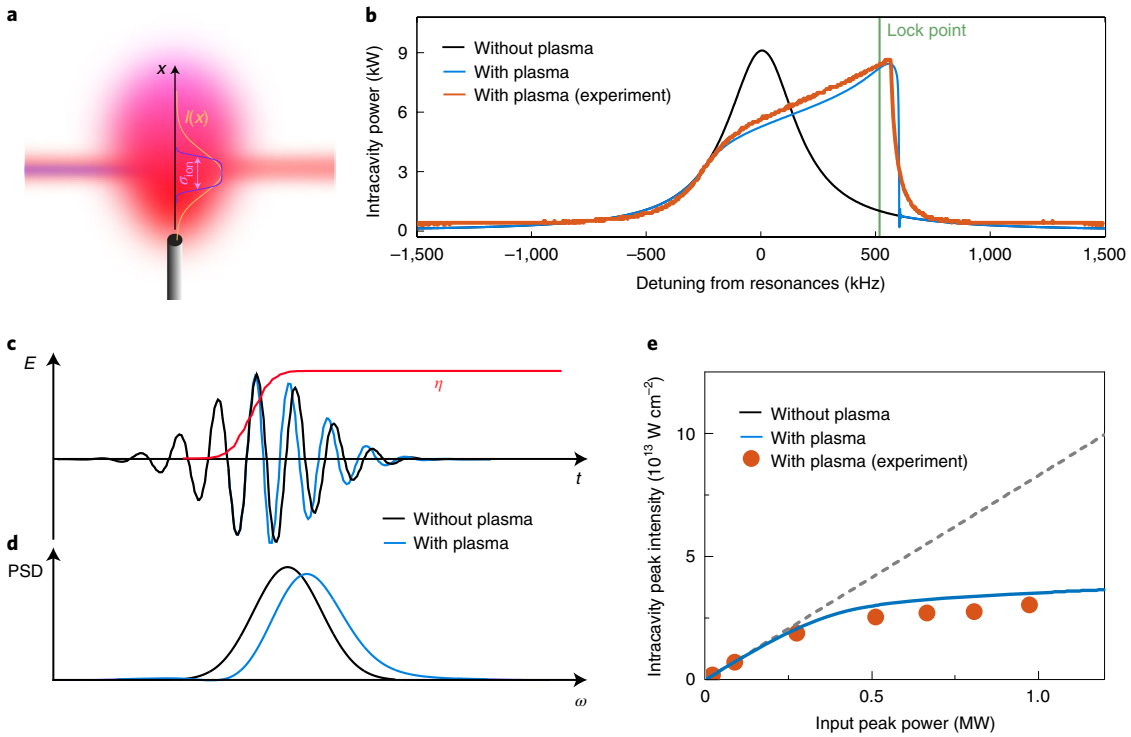

Fig. 3 | Nonlinearity-induced intensity limitations. a, The atoms of a (monatomic) gas mixture are accelerated from the nozzle exit and traverse the interaction region σ_{ion}, given by the full-width at half-maximum of the single-pulse ionization-fraction profile $\eta(x)$, asymptotically approaching the terminal velocity[115] $v(x) = \sqrt{5R_gT_g/M_{avg}}$, where R_g is the gas constant, T_g is the reservoir temperature and M_{avg} is the average molar mass, and the final ionization fraction depends on the driving pulse intensity $I(x)$. Neglecting plasma expansion, each atom is hit by $N = \frac{\sigma_{ion}}{vT_r}$ pulses, where T_r is the pulse repetition period. **b**, When the detuning between the frequency-comb lines and the cavity resonances is scanned towards higher frequencies, for example, by decreasing the cavity length, the intracavity power (blue) reaches its maximum at a different position than without plasma (grey), the dominant effect being the build-up of a cumulative plasma. This maximum cannot be reached by scanning in the opposite direction, that is, for each detuning there are at least two steady-state solutions, one with high power and one with low power[66,69]. To avoid this optical bistability and achieve a stable lock, the lock point must be set slightly before the maximum (green), after which the high- and low-power branches unite[66]. **c**, The electric field of an intense pulse before (black) and after (blue) passing through an ionizing medium, leading to temporal compression due to the time-dependent plasma refractive index $n(t)$. **d**, In the frequency domain, this corresponds to a spectral blueshift[133], reducing the spectral overlap with the seeding pulses. PSD, (optical) power spectral density. **e**, As a consequence, the intracavity power shows a saturation behaviour when the seeding power is increased (intensity clamping). Panels adapted with permission from: **b**, ref. [69], APS; **e**, ref. [63], APS.

the plate surface, a fraction of the XUV beam is coupled out from the cavity[34–36,44,48,49,54] (Fig. 4a). While excessive dispersion can (for typical finesse values) be avoided by using adequately thin plates, nonlinear effects in the plate material hamper the peak-power scalability[44], and thermal lensing can complicate operation. This method has been applied for XUV photon energies up to 42 eV (ref. [44]) and typically provides 5–15% output coupling efficiency.

Another successful method for (frequency domain) applications where angular dispersion of the harmonics is acceptable (or even desirable) is to use a reflective XUV diffraction grating (Fig. 4b) etched into the top layer of an fsEC mirror with high reflectivity for the fundamental beam[42,52,66,67,74]. Output coupling efficiencies up to 10% in the photon energy range below 20 eV have been demonstrated.

Geometric output coupling through an on-axis aperture in the cavity mirror following the nonlinear medium and employing the fundamental transverse mode of the cavity makes use of the generally much smaller divergence angle of the XUV compared with the driving beam[45,53,73] (Fig. 4c). The XUV radiation exits the cavity without spectral alterations, and output coupling efficiencies of up to 40% and photon energies up to 100 eV have been reported, without severe reduction of the enhancement due to losses at the aperture[45,53,55,75]. Furthermore, the all-reflective geometry and the large illuminated spot on the output coupler grant excellent average and peak-power scalability. Although in general there is a trade-off between optimal generation efficiency and output coupling efficiency[75], this method has altogether enabled record photon rates for attosecond PES without detectable space-charge distortions[45].

By tailoring the transverse mode to obtain an intensity minimum at the position of the output coupling aperture and an on-axis intensity maximum at the position of the medium (Fig. 4d,e), the acceptable diameter of the aperture can be substantially increased, so that high output coupling efficiency is possible (in particular for lower-order harmonics). This can be achieved by operating at a position in the stability range where two (or more) degenerate transverse modes combine to a resonant superposition[76] or by using a noncollinear setup[73]. Noncollinear methods allow for output coupling efficiencies beyond 50% and work well up to soft X-ray wavelengths[64]. Recently, with such a method, record power around 13 eV radiation has been demonstrated[77] (Fig. 4f). In addition, these schemes can also facilitate the implementation of wavefront-rotation-based generation of isolated attosecond pulses[64].

Several alternative concepts have been suggested; however, they have so far not been demonstrated experimentally. These include geometric output coupling using rotationally symmetric modes[73,78] and methods using an antireflection-coated grazing-incidence plate[79] or angular separation by a highly reflective mirror covered with a wedged layer[80].

Hydrocarbon contaminants in the vacuum chamber can be deposited on the optics during HHG generation and harm the performance[39]. Immersing the optics—in particular XUV output coupling optics—in ozone during operation cleans the hydrocarbons in situ and allows for stable fsEC operation for months of intensive use[43,44,64]. Occasionally, the optics can be cleaned in external reactive-ion etchers to remove any residual contaminants[52].

XUV frequency-comb stability and coherence

To ensure the resonant condition between the VIS/NIR comb and the fsEC, active control is required for the two degrees of freedom of the comb, ω_r and ω_0 (refs. [38,59,81]). The reflected light from the fsEC, dispersed by a grating, can be detected within a narrow (~1 nm) spectral window, to provide wavelength-selective, phase-sensitive information on the interference of the seeding with the circulating light. Typically, the Pound–Drever–Hall technique[82] is employed, where frequency modulation is applied to generate symmetric sidebands at each seeding comb mode, and the interference signal is demodulated to generate the corresponding error signal for feedback stabilization. The linear combination of two such error signals from different spectral regions can be used for a two-point lock[43,44,59]. Alternatively, the comb-offset frequency ω_0 can be locked to an external radiofrequency reference to match the optimum value for cavity enhancement, while a single error signal is used to stabilize ω_r or the geometrical fsEC length[45]. While the intrinsic stability of the comb or the fsEC is sufficient for many time-domain applications[43–45], additional stabilization of the VIS/NIR comb to absolute frequency standards[83] can be required for direct frequency determination in precision spectroscopy experiments[33,40,41].

The excessive relative intensity noise (RIN) of the XUV comb results mainly from amplitude fluctuations of the cavity-enhanced driving comb. At low frequencies within the servo-loop bandwidth for the cavity lock, typically a few tens of kilohertz, the intracavity comb RIN is limited by the RIN of the seed laser[84]. Beyond the feedback loop bandwidth, residual relative frequency noise between the comb and the fsEC is converted into RIN. Therefore, by minimizing the intensity and frequency noise of the seed laser and using a high-bandwidth feedback lock, the intensity noise of the XUV comb can effectively be reduced. Typically, an intensity noise on the order of 1% (root mean squared) can be obtained for the VIS/NIR intracavity light for measurement time up to hours[43,44,53,71,84]. Due to the highly nonlinear HHG process, this can result in a RIN of a few percent in the XUV output (Fig. 5a).

Optical phase coherence in the XUV is essential for precision spectroscopy. Since the first demonstrations of cavity-enhanced HHG[34,35], it has been a central question whether the seemingly violent HHG process can preserve the delicate optical phase coherence. In these pioneering works, phase coherence of the third harmonic from fsEC was demonstrated by optical heterodyne measurements. High-order harmonics, however, exhibit an intensity-dependent phase originating from the quantum electron trajectories during the HHG process[11]. Thus, intracavity VIS/NIR comb RIN is converted to XUV comb phase noise[85]. Usually, the on-axis harmonics originating from the short-trajectory contribution can be selected by phase matching and iris clipping. Theoretical estimations show that the intensity-to-phase noise conversion process has a negligible contribution on the XUV comb linewidth[85]. For example, 1% root-mean-squared RIN at a generation intensity of 2×10^{14} W cm^{-2}

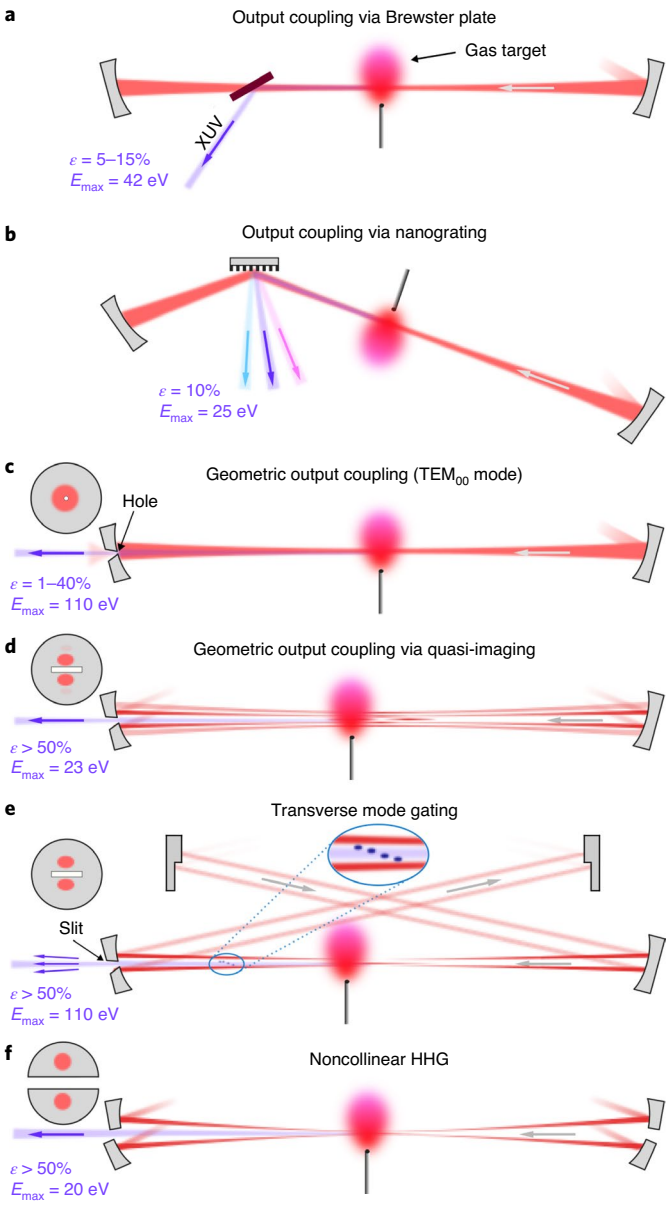

Fig. 4 | XUV output coupling methods. Typical efficiencies (ε) and maximum demonstrated photon energies E_{max}. **a**, A thin, transparent plate placed at Brewster's angle in the fundamental beam reflects a fraction of the collinearly propagating XUV beam. **b**, A reflective XUV diffraction grating, etched into the top layer of a highly reflective mirror for the fundamental beam, angularly disperses the individual harmonic orders. **c**, An on-axis aperture in the cavity mirror after the HHG focus allows for XUV output coupling using the fundamental Gauss–Hermite transverse electromagnetic cavity mode (TEM_{00}) without spectral alterations of either of the beams. **d**, By operating the resonator at a specific position in the stability range, several degenerate transverse modes overlap to form a tailored 'quasi-imaging' mode with an on-axis intensity minimum at the output coupling mirror, and an on-axis intensity maximum close to the HHG focus. **e**, For 'transverse mode gating', the Gauss–Hermite 01 mode, which has an on-axis intensity minimum, is modified by monolithically delaying one lobe with a stepped mirror, so that an on-axis maximum is obtained in the focal region. The alteration is reversed after the focus. Besides enabling high output coupling efficiency, this scheme can spatially gate isolated attosecond pulses (illustrated by the spatially dispersed beamlets in the inset). **f**, Noncollinear HHG uses two circulating pulses in the fundamental mode, intersecting at a common focal region with the same effect. This can be seen as a generalized geometry for transverse mode gating, where separate focusing mirrors are used for each lobe, introducing an additional degree of freedom that permits control of the crossing angle.

in a xenon target leads to only 0.12 rad root-mean-squared phase noise in the XUV, leaving >98% of the power in the optical carrier.

Experimental confirmation of the XUV comb structure was first achieved with pulse-to-pulse interference of the seventh harmonic[85], putting a <20 MHz upper bound for the XUV comb linewidth at 150 nm. Later, direct frequency-comb spectroscopy in argon and neon jets[40] at XUV wavelengths revealed a similar upper bound of <10 MHz comb linewidth, limited by the Doppler-broadened transition linewidth. The most stringent coherence test was achieved by a heterodyne measurement between two XUV combs, showing a long optical coherence time limited by the phase noise on the fundamental comb[36], and that sub-100 mHz XUV linewidth can be achieved. In that measurement, a NIR comb was split to generate two independent XUV combs in separate fsECs. This way, the common-mode phase noise of the fundamental comb was rejected except for some residual differential path-length noise, allowing one to investigate any decoherence effect in the cavity-enhanced HHG process with unprecedented precision.

For a noise-free frequency multiplication process, the optical phase of a comb line in the qth harmonic is given by $\phi_q = q \times \phi_1$. We approximate the 3 dB optical linewidth δf_q by the relation:

$$1\,\mathrm{rad}^2 = \int_{\delta f_q}^{\infty} S_{\phi,q}(f)\mathrm{d}f, \qquad (2)$$

where $S_{\phi,q} \propto \phi_q^2 \propto q^2$ is the phase noise power spectral density of a given comb line[36]. Assuming a relative optical linewidth dominated by white frequency noise due to path-length fluctuations in the heterodyne interferometer, one obtains $S_{\phi,q}(f) \propto 1/f^2$. Therefore, the corresponding XUV comb linewidth shows a quadratic scaling behaviour with respect to the harmonic order as $\delta f_q \propto q^2$ (Fig. 5b). When the relative path-length fluctuation was removed by active stabilization, a 62.5 mHz resolution-limited beat-note linewidth was demonstrated for the 17th harmonic, showing indeed no measurable phase noise added by the HHG process down to the sub-100 mHz regime[36] (Fig. 5b, insets). A more favourable linear linewidth scaling $\delta f_q \propto q$ is expected if the fundamental linewidth is dominated by flicker frequency noise $S_{\phi,q}(f) \propto 1/f^3$. Assuming the highest laser stability demonstrated so far with a sub-10 mHz linewidth dominated by flicker frequency noise[86], subhertz comb linewidth can potentially be achieved for all harmonic orders up to $q = 99$.

XUV frequency-comb spectroscopy

XUV frequency combs are key to high-resolution XUV spectroscopy[40,41] for probing fundamental physics. For example, precision spectroscopy of few-electron atoms[87,88] and ions (including highly charged ions)[89,90] in the XUV spectral region can provide stringent tests for quantum electrodynamics theory. Furthermore, XUV frequency combs offer a direct frequency link from XUV optical frequencies to ω_0 and ω_r in the radiofrequency domain. The spectroscopy targets typically exhibit sparse, isolated transition

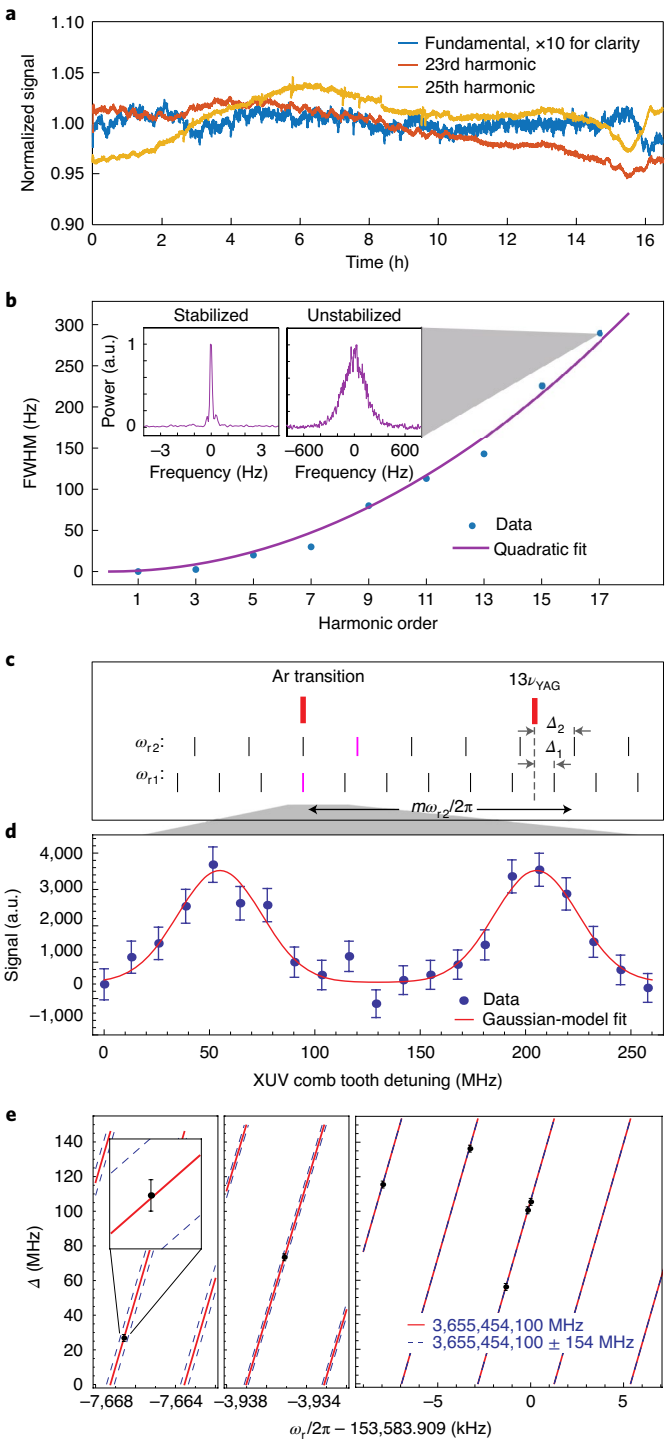

Fig. 5 | XUV frequency-comb coherence and spectroscopy. a, Long-term intensity stability of fsEC HHG. **b**, Quadratic scaling of XUV heterodyne beat-note linewidth, measured as full-width at half-maximum (FWHM), as a function of the harmonic order. Insets show the 17th harmonic beat notes, when the interferometer is stabilized (left, resolution bandwidth 62.5 mHz) or free-running (right, resolution bandwidth 30 Hz). **c**–**e**, Direct frequency-comb spectroscopy scheme and results of an argon transition at 82 nm. **c**, The experiment schematic. The two sets of black and purple lines represent XUV comb modes at two different repetition rates. The two purple lines represent the same comb mode that is shifted when changing the repetition rate from ω_{rep1} to ω_{rep2}. The scale is exaggerated for clarity. **d**, Measured fluorescence signal as a function of the frequency detuning of a comb mode (purple line in **c**), normalized by the XUV flux. Error bars are determined from the shot noise of fluorescence photons. The linewidth shown here is limited by Doppler broadening. **e**, Determination of the comb-mode number and, thus, of the absolute transition frequency. As the repetition frequency ω_r is tuned, multiple resonances are recorded (black data points). Red lines show the expected resonance position for the correct comb-mode number assignment m. Blue dashed lines correspond to $m \pm 1$. The magnified inset shows that the measurement error is sufficiently small to determine the mode number unambiguously (the error bar represents the standard deviation). Figure adapted with permission from: **a**, ref. [43], AIP; **b**, ref. [36], Springer Nature Ltd; **c**–**e**, ref. [40], Springer Nature Ltd.

lines[87–89,91], allowing for the determination of their frequencies via direct frequency-comb spectroscopy[40,41]. The excitation rate of the transition can be monitored, typically by fluorescence or ionization, to determine when a single comb line is tuned into resonance. Multiple measurements of the resonance with different ω_r can be used to determine the comb-mode number and, therefore, the absolute transition frequency, without requiring a spectrometer.

With steady progress in building robust XUV combs with increasing spectral power, proof-of-principle direct frequency-comb spectroscopy measurements with XUV combs have emerged, demonstrating unprecedented spectral resolution and accuracy. An electric dipole transition in argon with frequency $\nu_{Ar} \approx 3.653 \times 10^{15}$ Hz (corresponding to 82 nm) was determined with an uncertainty of 6 MHz by the intracavity-generated 13th harmonic of a Yb-fibre comb[40]. In this experiment, an iodine-stabilized neodymium-doped yttrium aluminium garnet (Nd:YAG) laser with a known frequency ν_{YAG} was used as an optical frequency reference[92]. The comb repetition frequency ω_r was stabilized by phase-locking the beat frequency between one comb line and ν_{YAG} to a radiofrequency δ. The absolute value of ω_r was determined by a frequency counter. The comb-offset frequency ω_0 was passively tuned to optimize the cavity enhancement; yet, it was otherwise free-running with a 15 kHz linewidth. The optical frequency ν_m of an XUV comb mode can thus be determined by:

$$\nu_m = m \times \omega_r/2\pi + 13\nu_{YAG} + \Delta, \quad (3)$$

where $\Delta = 13 \times \delta (\text{modulo}\, \omega_r/2\pi)$ and m is the number of comb spacings between the mode m and the XUV frequency at $13\nu_{YAG} + \Delta$ (Fig. 5c).

In the case of resonant excitation, that is, $\nu_m = \nu_{Ar}$, fluorescence is generally detected using a photomultiplier tube. With 10 pW per mode of XUV light delivered to the spectroscopy target, fluorescence detection has allowed for a signal-to-background ratio between 0.5 and 1.0. A nearly 100% contrast was obtained when the background photons were subtracted using their timing information (Fig. 5d). To determine the absolute transition frequency, at least two measurements are required at different ω_r while keeping track of the change in the resonant comb-mode index Δm (Fig. 5c). For the experimentally determined offset Δ with an uncertainty σ_Δ, the integer comb-mode number m can be uniquely determined provided that $2\sqrt{2}\pi\sigma_\Delta/(\omega_{r1} - \omega_{r2}) < 1$ holds, where $\omega_{r1} - \omega_{r2}$ is the change in the repetition frequency. In practice, ω_r was tuned with increasing step size to keep Δm trackable. Figure 5e shows the unambiguous assignment of the absolute comb-mode number.

In another experimental demonstration of XUV frequency-comb spectroscopy[41], the 7th harmonic of a Yb-fibre comb was used to excite a transition in xenon around 147 nm. Again, time-resolved fluorescent photon counts enabled efficient removal of the background, thereby allowing spectroscopy measurement with only 500 fW per XUV mode. In this case, the repetition frequency tuning range $\Delta\omega_r$, limited by technical issues, was not large enough to unambiguously determine the comb-mode number m. Nevertheless, a probability distribution of m was determined from the limited tuning range, resulting in a frequency uncertainty of 280 MHz.

Although direct XUV frequency-comb spectroscopy has so far only been demonstrated with Doppler-limited transitions in gas jets, its potential application to much narrower transitions offers truly exciting prospects for fundamental physics. Recent advances in the generation[45,52] and output coupling efficiencies[75,77] enabled the boost of the XUV power directly available for spectroscopy to >1 nW per mode, which opens the door for 'photon hungry' spectroscopy experiments. In particular, spectroscopy of ^{229}Th with a single XUV comb line[93] could potentially lead to the development of highly stable and portable nuclear-based optical clocks.

Direct XUV frequency-comb spectroscopy has also been proposed for two-photon transitions[88,89], where pairs of comb lines are combined to excite the transition, thereby efficiently using the entire comb average power and potentially allowing for Doppler-free spectroscopy measurements. Time-averaged XUV comb powers per harmonic in the range between 1 and 100 μW, which are available from modern fsECs[52], are considered sufficient for these purposes (depending on the exact experimental scheme).

Megahertz-repetition-rate PES and attosecond physics

Another field of application that has motivated the development of high-flux, high-photon-energy multimegahertz HHG sources has been multidimensional PES. Measurements of angularly or spatially resolved photoemission spectra with high kinetic-energy resolution and, in the case of pump–probe experiments in dependence of the delay between a pump and a probe pulse, inherently demand the recording of a large number of photoelectrons. However, Coulomb interaction of multiple photoelectrons released from the sample during a single pulse affects their velocities and trajectories towards the detector, distorting the observables[26,94,95] and thus, limiting the number of photo-released electrons affordable per pulse. In fact, in most state-of-the-art kilohertz-repetition-rate setups for multidimensional PES on solids, space-charge effects require a considerable attenuation of the photon flux available from the source[21,26,45]. With travel times of only nanoseconds for the photoelectrons to reach the detector, the detection duty cycle amounts to a fraction of a percent[45], implying impractical (or even prohibitive) measurement times of several days. For comparison, third-generation synchrotrons emit pulsed radiation with repetition rates of several hundreds of megahertz, set by the temporal spacing of the electron bunches[96]—but are limited in accessibility, and do not provide (sub) femtosecond temporal resolution.

Recently, first experiments[42–45,97] employing cavity-enhanced Yb-fibre-based femtosecond frontends have showcased a number of benefits of multikilowatt-average-power, multimegahertz-repetition-rate HHG in xenon, krypton, argon and neon for low-space-charge PES, at photon rates similar to those of state-of-the-art kilohertz systems (Fig. 1), and up to within one order of magnitude of those used in synchrotron beamlines dedicated to monochromatic PES experiments[96,98]. With 120 fs pulses circulating at a repetition rate of 60 MHz, tunable HHG in the 8 to 40 eV photon-energy range has been reported, with about 10^{11} photons per second from the 21st harmonic (25 eV) delivered to a $400 \times 200\,\mu m^2$ spot onto solid-state samples[42,43]. An energy resolution as low as 22 meV was determined in the measurement despite the high photon flux (Fig. 6a,b).

In the past two decades, several pump–probe spectroscopic techniques with temporal resolution down to the attosecond regime, harnessing HHG, have emerged. Typically, ultrafast dynamics are initiated in a sample by either the visible/infrared pulse driving the HHG or the XUV high-harmonic pulse. Among the various ways in which the temporal evolution of these dynamics is probed[99], PES provides perhaps the most direct experimental access to the electronic wavefunctions. In addition, PES affords the fundamental advantage over all-optical spectroscopies of its spatial resolution being limited by the de Broglie wavelength of the detected electrons.

Employing an fsEC system with similar parameters (155 fs pulses circulating at 88 MHz, $>10^{11}$ photons per second delivered to a $58 \times 100\,\mu m^2$ spot, tunable in the 18 to 37 eV range), a sideband in the photoelectron spectrum associated with the laser-assisted photoelectric effect (LAPE), with an amplitude as low as 10^{-4} relative to the peak of the XUV-only induced spectrum, was measured on the timescale of several minutes[44] (Fig. 6c). This demonstrates the high quality of LAPE spectra attainable with high-flux radiation sources at space-charge effects below the detection limit. In particular, the ability to detect weak dressing fields (Fig. 6d)

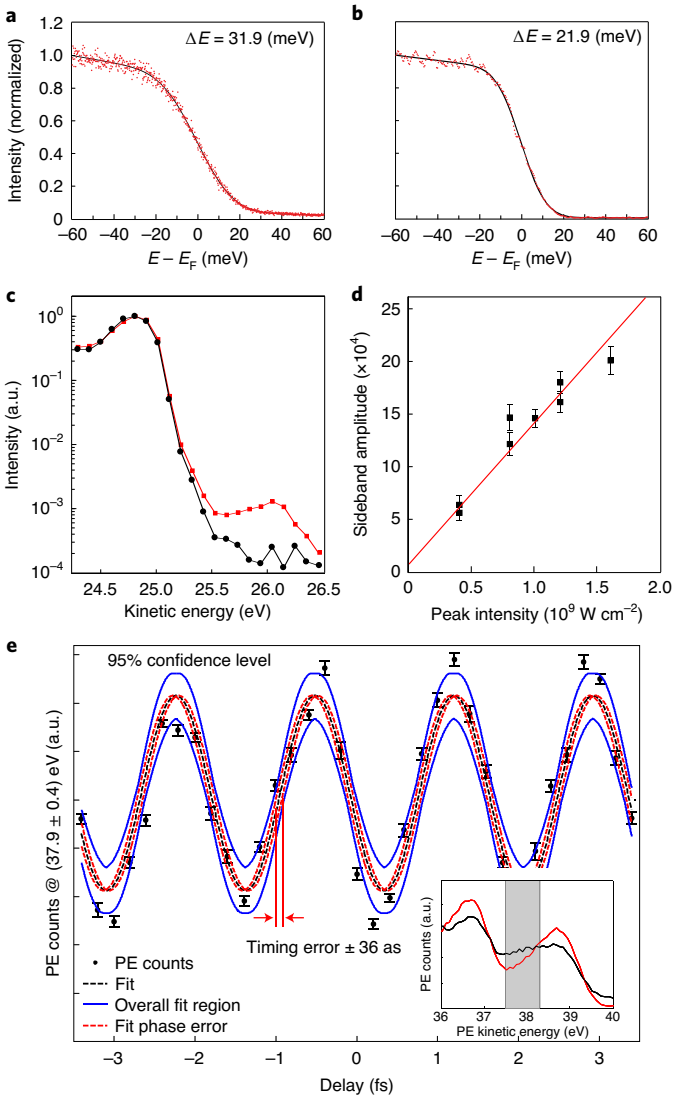

Fig. 6 | PES employing cavity-enhanced HHG. a,**b**, Fermi edge (E_F) measurements at 4.5 K on freshly evaporated gold, performed with 25 eV photon energy without (**a**) and with (**b**) a spectrally selective slit in the spectrally dispersed XUV beam. The fit represents a Fermi–Dirac function convolved with a Gaussian, yielding the energy resolution ΔE. In **b**, the photoelectron count is reduced by ~25% with respect to **a**. **c**,**d**, Photoelectron spectra of the gold Fermi edge without (black) and with (red) a 1.035 µm pump pulse impinging on the sample simultaneously with the XUV beam, at a peak intensity as low as 1.3×10^9 W cm^{-2} (**c**), and relative amplitude of the LAPE sideband as a function of the pump pulse intensity (**d**). The linear behaviour of the latter attests to weak space-charge distortions and to the ability to perform LAPE measurements at weak pump field strengths. The error bars reflect statistics over several measurements. **e**, Intensity of the LAPE sideband at 37.9 eV photoelectron (PE) kinetic energy, obtained from a W(110) crystal probed with high harmonics generated in argon and pumped by the variably delayed collinearly propagating 1.03 µm, 40 fs pulse, recorded within a measurement time of 105 s. The phase fit error (red dashed line) corresponds to 36 as and is comparable to the timing jitter of the interferometer[45]. Blue lines, maximum and minimum error boundaries of all fit parameters. The error bars indicate the 95% confidence level. The inset shows photoelectron spectra at two different delays with (black) and without (red) sideband and the region over which the sideband intensity was integrated (grey). Panels **a** and **b** reproduced with permission from ref. [43], AIP. Panels adapted with permission from **c**,**d**, ref. [44], AIP; **e**, ref. [45], Springer Nature Ltd.

will benefit, for example, the observation of plasmonic surface fields with a high dynamic range[24,25,100]. The temporal resolution in these two aforementioned pioneering works[43,44] was restricted to >100 fs by the relatively narrow XUV bandwidth, necessary for PES with high kinetic-energy resolution. While this suffices to study phenomena such as electron–phonon dynamics[43,96], electron–electron interactions occur on much shorter timescales. The subfemtosecond coherent dynamics of HHG can be leveraged to access these via LAPE. In particular, the RABBITT[101,102] technique (reconstruction of attosecond harmonic beating by interference of two-photon transitions), using the trains of attosecond pulses generated by driving HHG with multicycle optical fields, enables a unique combination of attosecond temporal resolution (owing to the brevity of the individual attosecond pulses in the train) with narrowband spectral excitation stemming from spectrally isolated harmonics rather than a continuous spectrum[103]. Very recently, the potential of this combination for the investigation of electron dynamics in condensed matter has been demonstrated employing single-pass, kilohertz-repetition-rate HHG for angle-resolved RABBITT measurements on metals, revealing differences in the lifetimes between photoelectrons born into free-electron-like states and those excited into unoccupied excited states[23], highlighting the differences in fundamental electron–electron interactions, such as scattering and screening[21].

The multicycle nature of pulses typically employed for fsEC HHG renders them ideally suited for such experiments. In a recent proof-of-principle experiment[45], the entire 20 to 60 eV harmonic spectrum generated in argon (and up to ~100 eV generated in neon) by 40 fs pulses at 18.4 MHz, together with the collinearly co-propagating fundamental beam, was geometrically output coupled through an on-axis aperture in the mirror after the HHG focus. The LAPE sideband modulation shown in Fig. 6e demonstrates a temporal resolution on the order of a few tens of attoseconds. For these measurements, up to 10^{10} photoelectrons per second were released from a 10-µm-diameter spot on a tungsten sample without noticeable space-charge distortions. Employing an angle-resolving time-of-flight photoelectron detector enabled the collection of nearly all photoelectrons of interest, at a temporal duty cycle close to 100% (to this end, the repetition rate of HHG was matched to the time of flight)[45]. This results in acquisition times of a few minutes for time-, angle- and kinetic-energy-resolved photoelectron spectra with high signal-to-noise ratios, heralding a new regime for RABBITT-based measurements.

While the extension of fsEC HHG to the generation of temporally isolated attosecond pulses, enabling attosecond streaking[12,14,15,19,24] at multimegahertz repetition rates, has not yet been demonstrated, important milestones in this direction have been achieved. A theoretical study[104] has identified tailoring the transverse field distribution of the HHG driving pulse as a promising strategy. Experimental demonstrations of the passive enhancement of waveform-stable pulses (that is, offset-free frequency combs)[65] and sub-20 fs near-infrared pulses[58] to kilowatt average powers, and a first demonstration of fsEC HHG with a rotating wavefront[64] promise the feasibility of efficient generation of isolated attosecond pulses with fsECs.

Conclusions and outlook

Cavity-enhanced HHG has reached a maturity that allows for both time-domain studies and frequency-domain precision metrology in unprecedented regimes. In particular, the energy of femtosecond pulses emitted by 100-W-average-power-level, near-infrared frequency combs can be passively enhanced in fsECs by factors >30, allowing for HHG with intracavity conversion efficiencies on the order of those achieved in single-pass geometries with similar gas targets, with robust operation over many hours now being routinely achieved.

Rigorous proof of the HHG coherence[36] along with first direct frequency-comb demonstration experiments[40,41] have opened the door to precision spectroscopy in the vast XUV spectral region of fundamental physical interest. A particularly exciting prospect is direct XUV comb spectroscopy of the ^{229}Th nuclear transition. Recent developments in nuclear physics[91] constrained the isomeric excited state energy of ^{229}Th nucleus to 8.12 ± 0.11 eV, rendering direct nuclear laser spectroscopy and even a nuclear-based optical clock with an XUV frequency comb possible. A nuclear-transition clock[105] will have suppressed field-induced frequency shifts, as the nucleus interacts only via the relatively small nuclear moments and is highly isolated from the environment. It is also expected to offer unprecedented sensitivity (enhanced by several orders of magnitude compared with atomic references) for temporal variations of fundamental constants such as the fine structure constant α and the dimensionless strong interaction scalar parameter m_q/Λ_{QCD}, where m_q is the light quark mass and Λ_{QCD} is the quantum chromodynamics scale, testing our understanding of fundamental physics[106]. The future combination of the XUV comb with Fourier-transform spectroscopy or dual-comb spectroscopy techniques can potentially enable broadband comb-mode-resolved spectroscopy in the XUV.

For PES, the original impetus for the development of fsEC HHG was the prospect of mitigating space-charge effects in photoemission from condensed matter. Experiments have recently shown that fsEC technology has kept this promise[43–45,97] demonstrating PES in a unique parameter regime, combining high XUV photon energies with high photon rates and high kinetic-energy resolution. With access to this new regime, advances in material and surface science[19–23,107–109] become likely as well as future technologies such as light-wave-driven signal processing at petahertz clock rates[100,110]. The combination of cavity-enhanced HHG with photoelectron emission microscopy might enable 'filming' nanoplasmonic surface fields with attosecond and nanometre temporal and spatial resolution[24,100]. Other metrologies such as transient-absorption spectroscopy[111], HHG spectroscopy[112] or coherent diffraction imaging[113] are likely to benefit from the new regime of multimegahertz-repetition-rate HHG.

Future developments of fsEC technology will undoubtedly continue to nourish an ever-growing spectrum of spectroscopy and microscopy applications. In particular, novel, power-scalable geometric XUV output coupling methods promise >50% efficiencies, as well as the generation of broadband, isolated XUV pulses. Newly emerging, high-power Tm-fibre-based frequency combs[114] emitting around 2 μm promise efficient generation of water-window harmonics in fsECs due to the ponderomotive scaling of HHG in gases, thus opening up new regimes of coherent XUV sources.

Received: 26 May 2020; Accepted: 19 November 2020;
Published online: 28 January 2021

References

1. Haus, H. A. Mode-locking of lasers. *IEEE J. Sel. Top. Quantum Electron.* **6**, 1173–1185 (2000).
2. Zewail, A. H. Femtochemistry: atomic-scale dynamics of the chemical bond. *J. Phys. Chem. A* **104**, 5660–5694 (2000).
3. Reichert, J., Holzwarth, R., Udem, T. H. & Hänsch, T. W. Measuring the frequency of light with mode-locked lasers. *Opt. Commun.* **172**, 59–68 (1999).
4. Telle, H. R. et al. Carrier-envelope offset phase control: a novel concept for absolute optical frequency measurement and ultrashort pulse generation. *Appl. Phys. B* **69**, 327–332 (1999).
5. Apolonski, A. et al. Controlling the phase evolution of few-cycle light pulses. *Phys. Rev. Lett.* **85**, 740–743 (2000).
6. Jones, D. J. et al. Carrier-envelope phase control of femtosecond mode-locked lasers and direct optical frequency synthesis. *Science* **288**, 635–639 (2000).
7. Brabec, T. & Krausz, F. Intense few-cycle laser fields: frontiers of nonlinear optics. *Rev. Mod. Phys.* **72**, 545–591 (2000).
8. Agostini, P., Fabre, F., Mainfray, G., Petite, G. & Rahman, N. K. Free–free transitions following six-photon ionization of xenon atoms. *Phys. Rev. Lett.* **42**, 1127–1130 (1979).
9. Macklin, J. J., Kmetec, J. D. & Gordon, C. L. High-order harmonic generation using intense femtosecond pulses. *Phys. Rev. Lett.* **70**, 766–769 (1993).
10. Corkum, P. B. Plasma perspective on strong field multiphoton ionization. *Phys. Rev. Lett.* **71**, 1994–1997 (1993).
11. Lewenstein, M. et al. Theory of high-harmonic generation by low-frequency laser fields. *Phys. Rev. A* **49**, 2117–2132 (1994).
12. Krausz, F. & Ivanov, M. Attosecond physics. *Rev. Mod. Phys.* **81**, 163–234 (2009).
13. Hentschel, M. et al. Attosecond metrology. *Nature* **414**, 509–513 (2001).
14. Itatani, J. et al. Attosecond streak camera. *Phys. Rev. Lett.* **88**, 173903 (2002).
15. Kienberger, R. et al. Atomic transient recorder. *Nature* **427**, 817–821 (2004).
16. Uiberacker, M. et al. Attosecond real-time observation of electron tunnelling in atoms. *Nature* **446**, 627–632 (2007).
17. Baker, S. et al. Probing proton dynamics in molecules on an attosecond time scale. *Science* **312**, 424–427 (2006).
18. Schell, F. et al. Molecular orbital imprint in laser-driven electron recollision. *Sci. Adv.* **4**, eaap8148 (2018).
19. Cavalieri, A. L. et al. Attosecond spectroscopy in condensed matter. *Nature* **449**, 1029–1032 (2007).
20. Locher, R. et al. Energy-dependent photoemission delays from noble metal surfaces by attosecond interferometry. *Optica* **2**, 405–410 (2015).
21. Chen, C. et al. Distinguishing attosecond electron–electron scattering and screening in transition metals. *Proc. Natl Acad. Sci. USA* **114**, E5300–E5307 (2017).
22. Ambrosio, M. J. & Thumm, U. Electronic structure effects in spatiotemporally resolved photoemission interferograms of copper surfaces. *Phys. Rev. A* **96**, 051403 (2017).
23. Tao, Z. et al. Direct time-domain observation of attosecond final-state lifetimes in photoemission from solids. *Science* **353**, 62–67 (2016).
24. Stockman, M. I., Kling, M. F., Kleineberg, U. & Krausz, F. Attosecond nanoplasmonic-field microscope. *Nat. Photon.* **1**, 539–544 (2007).
25. Förg, B. et al. Attosecond nanoscale near-field sampling. *Nat. Commun.* **7**, 11717 (2016).
26. Chew, S. H. et al. Time-of-flight-photoelectron emission microscopy on plasmonic structures using attosecond extreme ultraviolet pulses. *Appl. Phys. Lett.* **100**, 051904 (2012).
27. Udem, T., Holzwarth, R. & Hänsch, T. W. Optical frequency metrology. *Nature* **416**, 233–237 (2002).
28. Ye, J. & Cundiff, S. T. *Femtosecond Optical Frequency Comb: Principle, Operation, and Applications* (Springer, 2005).
29. Riehle, F., Gill, P., Arias, F. & Robertsson, L. The CIPM list of recommended frequency standard values: guidelines and procedures. *Metrologia* **55**, 188–200 (2018).
30. Oelker, E. et al. Demonstration of 4.8×10^{-17} stability at 1 s for two independent optical clocks. *Nat. Photon.* **13**, 714–719 (2019).
31. Marian, A., Stowe, M. C., Lawall, J. R., Felinto, D. & Ye, J. United time-frequency spectroscopy for dynamics and global structure. *Science* **306**, 2063–2068 (2004).
32. Thorpe, M. J., Moll, K. D., Jones, R. J., Safdi, B. & Ye, J. Broadband cavity ringdown spectroscopy for sensitive and rapid molecular detection. *Science* **311**, 1595–1599 (2006).
33. Picqué, N. & Hänsch, T. W. Frequency comb spectroscopy. *Nat. Photon.* **13**, 146–157 (2019).
34. Gohle, C. et al. A frequency comb in the extreme ultraviolet. *Nature* **436**, 234–237 (2005).
35. Jones, R. J., Moll, K. D., Thorpe, M. J. & Ye, J. Phase-coherent frequency combs in the vacuum ultraviolet via high-harmonic generation inside a femtosecond enhancement cavity. *Phys. Rev. Lett.* **94**, 193201 (2005).
36. Benko, C. et al. Extreme ultraviolet radiation with coherence time greater than 1 s. *Nat. Photon.* **8**, 530–536 (2014).
37. Jones, R. J. & Ye, J. Femtosecond pulse amplification by coherent addition in a passive optical cavity. *Opt. Lett.* **27**, 1848–1850 (2002).
38. Jones, R. J. & Ye, J. High-repetition-rate coherent femtosecond pulse amplification with an external passive optical cavity. *Opt. Lett.* **29**, 2812–2814 (2004).
39. Mills, A. K., Hammond, T. J., Lam, M. H. C. & Jones, D. J. XUV frequency combs via femtosecond enhancement cavities. *J. Phys. B* **45**, 142001 (2012).
40. Cingöz, A. et al. Direct frequency comb spectroscopy in the extreme ultraviolet. *Nature* **482**, 68–71 (2012).
41. Ozawa, A. & Kobayashi, Y. vuv frequency-comb spectroscopy of atomic xenon. *Phys. Rev. A* **87**, 022507 (2013).
42. Mills, A. K. et al. An XUV source using a femtosecond enhancement cavity for photoemission spectroscopy. *Proc. SPIE* **9512**, 95121I (2015).
43. Mills, A. K. et al. Cavity-enhanced high harmonic generation for extreme ultraviolet time- and angle-resolved photoemission spectroscopy. *Rev. Sci. Instrum.* **90**, 083001 (2019).

44. Corder, C. et al. Ultrafast extreme ultraviolet photoemission without space charge. *Struct. Dyn.* **5**, 054301 (2018).
45. Saule, T. et al. High-flux ultrafast extreme-ultraviolet photoemission spectroscopy at 18.4 MHz pulse repetition rate. *Nat. Commun.* **10**, 458 (2019).
46. Siegman, A. E. *Lasers* (University Science Books, 1986).
47. Thorpe, M. J., Jones, R. J., Moll, K. D., Ye, J. & Lalezari, R. Precise measurements of optical cavity dispersion and mirror coating properties via femtosecond combs. *Opt. Express* **13**, 882–888 (2005).
48. Ozawa, A. et al. High harmonic frequency combs for high resolution spectroscopy. *Phys. Rev. Lett.* **100**, 253901 (2008).
49. Lee, J., Carlson, D. R. & Jones, R. J. Optimizing intracavity high harmonic generation for XUV fs frequency combs. *Opt. Express* **19**, 23315–23326 (2011).
50. Hartl, I. et al. Cavity-enhanced similariton Yb-fiber laser frequency comb: 3×10^{14} W/cm^2 peak intensity at 136 MHz. *Opt. Lett.* **32**, 2870–2872 (2007).
51. Eidam, T., Röser, F., Schmidt, O., Limpert, J. & Tünnermann, A. 57 W, 27 fs pulses from a fiber laser system using nonlinear compression. *Appl. Phys. B* **92**, 9 (2008).
52. Porat, G. et al. Phase-matched extreme-ultraviolet frequency-comb generation. *Nat. Photon.* **12**, 387–391 (2018).
53. Pupeza, I. et al. Compact high-repetition-rate source of coherent 100 eV radiation. *Nat. Photon.* **7**, 608–612 (2013).
54. Ozawa, A., Zhao, Z., Kuwata-Gonokami, M. & Kobayashi, Y. High average power coherent vuv generation at 10 MHz repetition frequency by intracavity high harmonic generation. *Opt. Express* **23**, 15107–15118 (2015).
55. Carstens, H. et al. High-harmonic generation at 250 MHz with photon energies exceeding 100 eV. *Optica* **3**, 366–369 (2016).
56. Carstens, H. et al. Megawatt-scale average-power ultrashort pulses in an enhancement cavity. *Opt. Lett.* **39**, 2595–2598 (2014).
57. Carstens, H. et al. Large-mode enhancement cavities. *Opt. Express* **21**, 11606–11617 (2013).
58. Lilienfein, N. et al. Enhancement cavities for few-cycle pulses. *Opt. Lett.* **42**, 271–274 (2017).
59. Jones, R. J., Thomann, I. & Ye, J. Precision stabilization of femtosecond lasers to high-finesse optical cavities. *Phys. Rev. A* **69**, 051803 (2004).
60. Schliesser, A., Gohle, C., Udem, T. & Hänsch, T. W. Complete characterization of a broadband high-finesse cavity using an optical frequency comb. *Opt. Express* **14**, 5975–5983 (2006).
61. Pupeza, I. et al. Highly sensitive dispersion measurement of a high-power passive optical resonator using spatial-spectral interferometry. *Opt. Express* **18** 26184–26195 (2010).
62. Hammond, T. J., Mills, A. K. & Jones, D. J. Simple method to determine dispersion of high-finesse optical cavities. *Opt. Express* **17**, 8998–9005 (2009).
63. Holzberger, S. et al. Femtosecond enhancement cavities in the nonlinear regime. *Phys. Rev. Lett.* **115**, 023902 (2015).
64. Högner, M. et al. Cavity-enhanced noncollinear high-harmonic generation. *Opt. Express* **27**, 19675–19691 (2019).
65. Holzberger, S. et al. Enhancement cavities for zero-offset-frequency pulse trains. *Opt. Lett.* **40**, 2165–2168 (2015).
66. Yost, D. C. et al. Power optimization of XUV frequency combs for spectroscopy applications [Invited]. *Opt. Express* **19**, 23483–23493 (2011).
67. Hammond, T. J., Mills, A. K. & Jones, D. J. Near-threshold harmonics from a femtosecond enhancement cavity-based EUV source: effects of multiple quantum pathways on spatial profile and yield. *Opt. Express* **19**, 24871–24883 (2011).
68. Moll, K. D., Jones, R. J. & Ye, J. Nonlinear dynamics inside femtosecond enhancement cavities. *Opt. Express* **13**, 1672–1678 (2005).
69. Allison, T. K., Cingöz, A., Yost, D. C. & Ye, J. Extreme nonlinear optics in a femtosecond enhancement cavity. *Phys. Rev. Lett.* **107**, 183903 (2011).
70. Carlson, D. R., Lee, J., Mongelli, J., Wright, E. M. & Jones, R. J. Intracavity ionization and pulse formation in femtosecond enhancement cavities. *Opt. Lett.* **36**, 2991–2993 (2011).
71. Lilienfein, N. et al. Temporal solitons in free-space femtosecond enhancement cavities. *Nat. Photon.* **13**, 214–218 (2019).
72. Kalashnikov, V. L., Gohle, C. & Udem, T. Maximization of the ultrashort pulse power stored in a passive resonator synchronously pumped by a femtosecond oscillator. In *Advanced Solid-State Photonics, Technical Digest* 652–656 (Optical Society of America, 2005); https://doi.org/10.1364/ASSP.2005.MB2
73. Moll, K. D., Jones, R. J. & Ye, J. Output coupling methods for cavity-based high-harmonic generation. *Opt. Express* **14**, 8189–8197 (2006).
74. Yost, D. C., Schibli, T. R. & Ye, J. Efficient output coupling of intracavity high-harmonic generation. *Opt. Lett.* **33**, 1099–1101 (2008).
75. Högner, M., Saule, T. & Pupeza, I. Efficiency of cavity-enhanced high harmonic generation with geometric output coupling. *J. Phys. B* **52**, 075401 (2019).
76. Pupeza, I. et al. Cavity-enhanced high-harmonic generation with spatially tailored driving fields. *Phys. Rev. Lett.* **112**, 103902 (2014).
77. Zhang, C. et al. Noncollinear enhancement cavity for record-high out-coupling efficiency of an extreme-UV frequency comb. *Phys. Rev. Lett.* **125**, 093902 (2020).
78. Putnam, W. P., Schimpf, D. N., Abram, G. & Kärtner, F. X. Bessel–Gauss beam enhancement cavities for high-intensity applications. *Opt. Express* **20**, 24429–24443 (2012).
79. Pronin, O. et al. Ultrabroadband efficient intracavity XUV output coupler. *Opt. Express* **19**, 10232–10240 (2011).
80. Pupeza, I., Fill, E. E. & Krausz, F. Low-loss VIS/IR-XUV beam splitter for high-power applications. *Opt. Express* **19**, 12108–12118 (2011).
81. Jones, R. J. & Diels, J.-C. Stabilization of femtosecond lasers for optical frequency metrology and direct optical to radio frequency synthesis. *Phys. Rev. Lett.* **86**, 3288–3291 (2001).
82. Drever, R. W. P. et al. Laser phase and frequency stabilization using an optical resonator. *Appl. Phys. B* **31**, 97–105 (1983).
83. Schibli, T. R. et al. Optical frequency comb with submillihertz linewidth and more than 10 W average power. *Nat. Photon.* **2**, 355–359 (2008).
84. Li, X. et al. High-power ultrafast Yb:fiber laser frequency combs using commercially available components and basic fiber tools. *Rev. Sci. Instrum.* **87**, 093114 (2016).
85. Yost, D. C. et al. Vacuum-ultraviolet frequency combs from below-threshold harmonics. *Nat. Phys.* **5**, 815–820 (2009).
86. Matei, D. G. et al. 1.5 µm lasers with sub-10 mHz linewidth. *Phys. Rev. Lett.* **118**, 263202 (2017).
87. Bergeson, S. D. et al. Measurement of the He ground state lamb shift via the two-photon 1^1S-2^1S transition. *Phys. Rev. Lett.* **80**, 3475–3478 (1998).
88. Eyler, E. E. et al. Prospects for precision measurements of atomic helium using direct frequency comb spectroscopy. *Eur. Phys. J. D* **48**, 43–55 (2008).
89. Herrmann, M. et al. Feasibility of coherent xuv spectroscopy on the 1S–2S transition in singly ionized helium. *Phys. Rev. A* **79**, 052505 (2009).
90. Nauta, J. et al. Towards precision measurements on highly charged ions using a high harmonic generation frequency comb. *Nucl. Instrum. Methods Phys. Res. B* **408**, 285–288 (2017).
91. von der Wense, L. & Seiferle, B. The ^{229}Th isomer: prospects for a nuclear optical clock. *Eur. Phys. J. A* **56**, 277 (2020).
92. Ye, J., Ma, L. S. & Hall, J. L. Molecular iodine clock. *Phys. Rev. Lett.* **87**, 270801 (2001).
93. von der Wense, L. & Zhang, C. Concepts for direct frequency-comb spectroscopy of ^{229m}Th and an internal-conversion-based solid-state nuclear clock. *Eur. Phys. J. D* **74**, 146 (2020).
94. Hellmann, S., Rossnagel, K., Marczynski-Bühlow, M. & Kipp, L. Vacuum space-charge effects in solid-state photoemission. *Phys. Rev. B* **79**, 035402 (2009).
95. Buckanie, N. M. et al. Space charge effects in photoemission electron microscopy using amplified femtosecond laser pulses. *J. Phys. Condens. Matter* **21**, 314003 (2009).
96. Yamamoto, S. & Matsuda, I. Time-resolved photoelectron spectroscopies using synchrotron radiation: past, present, and future. *J. Phys. Soc. Jpn* **82**, 021003 (2013).
97. Na, M. X. et al. Direct determination of mode-projected electron–phonon coupling in the time domain. *Science* **366**, 1231–1236 (2019).
98. Iwasawa, H. et al. Rotatable high-resolution ARPES system for tunable linear-polarization geometry. *J. Synchrotron Radiat.* **24**, 836–841 (2017).
99. Kraus, P. M., Zürch, M., Cushing, S. K., Neumark, D. M. & Leone, S. R. The ultrafast X-ray spectroscopic revolution in chemical dynamics. *Nat. Rev. Chem.* **2**, 82–94 (2018).
100. Schoetz, J. et al. Perspective on petahertz electronics and attosecond nanoscopy. *ACS Photon.* **6**, 3057–3069 (2019).
101. Paul, P. M. et al. Observation of a train of attosecond pulses from high harmonic generation. *Science* **292**, 1689–1692 (2001).
102. Muller, H. G. Reconstruction of attosecond harmonic beating by interference of two-photon transitions. *Appl. Phys. B* **74**, s17–s21 (2002).
103. Isinger, M. et al. Photoionization in the time and frequency domain. *Science* **358**, 893–896 (2017).
104. Högner, M., Tosa, V. & Pupeza, I. Generation of isolated attosecond pulses with enhancement cavities—a theoretical study. *New J. Phys.* **19**, 033040 (2017).
105. Peik, E. & Tamm, C. Nuclear laser spectroscopy of the 3.5 eV transition in Th-229. *Europhys. Lett.* **61**, 181–186 (2003).
106. Berengut, J. C. & Flambaum, V. V. Testing time-variation of fundamental constants using a ^{229}Th nuclear clock. *Nucl. Phys. News* **20**, 19–22 (2010).
107. Cilento, F. et al. Dynamics of correlation-frozen antinodal quasiparticles in superconducting cuprates. *Sci. Adv.* **4**, eaar1998 (2018).
108. Rohwer, T. et al. Collapse of long-range charge order tracked by time-resolved photoemission at high momenta. *Nature* **471**, 490–493 (2011).

109. Boschini, F. et al. Collapse of superconductivity in cuprates via ultrafast quenching of phase coherence. *Nat. Mater.* **17**, 416–420 (2018).
110. Krausz, F. & Stockman, M. I. Attosecond metrology: from electron capture to future signal processing. *Nat. Photon.* **8**, 205–213 (2014).
111. Geneaux, R., Marroux, H. J. B., Guggenmos, A., Neumark, D. M. & Leone, S. R. Transient absorption spectroscopy using high harmonic generation: a review of ultrafast X-ray dynamics in molecules and solids. *Phil. Trans. R. Soc. A* **377**, 20170463 (2019).
112. Marangos, J. P. Development of high harmonic generation spectroscopy of organic molecules and biomolecules. *J. Phys. B* **49**, 132001 (2016).
113. Rothhardt, J., Tadesse, G. K., Eschen, W. & Limpert, J. Table-top nanoscale coherent imaging with XUV light. *J. Opt.* **20**, 113001 (2018).
114. Gaida, C. et al. High-power frequency comb at 2 µm wavelength emitted by a Tm-doped fiber laser system. *Opt. Lett.* **43**, 5178–5181 (2018).
115. Scoles, G. et al. *Atomic and Molecular Beam Methods* Vol. I (Oxford Univ. Press, 1988).
116. Takahashi, E. J., Nabekawa, Y. & Midorikawa, K. Low-divergence coherent soft X-ray source at 13nm by high-order harmonics. *Appl. Phys. Lett.* **84**, 4–6 (2004).
117. Takahashi, E. J. et al. Generation of strong optical field in soft X-ray region by using high-order harmonics. *IEEE J. Sel. Top. Quantum Electron.* **10**, 1315–1328 (2004).
118. Constant, E. et al. Optimizing high harmonic generation in absorbing gases: model and experiment. *Phys. Rev. Lett.* **82**, 1668–1671 (1999).
119. Ding, C. et al. High flux coherent super-continuum soft X-ray source driven by a single-stage, 10mJ, Ti:sapphire amplifier-pumped OPA. *Opt. Express* **22**, 6194–6202 (2014).
120. Lorek, E. et al. High-order harmonic generation using a high-repetition-rate turnkey laser. *Rev. Sci. Instrum.* **85**, 123106 (2014).
121. Rothhardt, J. et al. High-repetition-rate and high-photon-flux 70 eV high-harmonic source for coincidence ion imaging of gas-phase molecules. *Opt. Express* **24**, 18133–18147 (2016).
122. Klas, R. et al. Table-top milliwatt-class extreme ultraviolet high harmonic light source. *Optica* **3**, 1167–1170 (2016).
123. Rothhardt, J. et al. 53W average power few-cycle fiber laser system generating soft X rays up to the water window. *Opt. Lett.* **39**, 5224–5227 (2014).
124. Rothhardt, J. et al. Absorption-limited and phase-matched high harmonic generation in the tight focusing regime. *New J. Phys.* **16**, 033022 (2014).
125. Puppin, M. et al. Time- and angle-resolved photoemission spectroscopy of solids in the extreme ultraviolet at 500 kHz repetition rate. *Rev. Sci. Instrum.* **90**, 023104 (2019).
126. Hädrich, S. et al. High photon flux table-top coherent extreme-ultraviolet source. *Nat. Photon.* **8**, 779–783 (2014).
127. Chiang, C.-T. et al. Boosting laboratory photoelectron spectroscopy by megahertz high-order harmonics. *New J. Phys.* **17**, 013035 (2015).
128. Zhao, Z. & Kobayashi, Y. Realization of a mW-level 10.7-eV (λ=115.6nm) laser by cascaded third harmonic generation of a Yb:fiber CPA laser at 1-MHz. *Opt. Express* **25**, 13517–13526 (2017).
129. Emaury, F., Diebold, A., Saraceno, C. J. & Keller, U. Compact extreme ultraviolet source at megahertz pulse repetition rate with a low-noise ultrafast thin-disk laser oscillator. *Optica* **2**, 980–984 (2015).
130. Hädrich, S. et al. Exploring new avenues in high repetition rate table-top coherent extreme ultraviolet sources. *Light Sci. Appl.* **4**, e320–e320 (2015).
131. Vernaleken, A. et al. Single-pass high-harmonic generation at 20.8MHz repetition rate. *Opt. Lett.* **36**, 3428–3430 (2011).
132. Bernhardt, B. et al. Vacuum ultraviolet frequency combs generated by a femtosecond enhancement cavity in the visible. *Opt. Lett.* **37**, 503–505 (2012).
133. Penetrante, B. M., Wood, W. M., Siders, C. W., Bardsley, J. N. & Downer, M. C. Ionization-induced frequency shifts in intense femtosecond laser pulses. *J. Opt. Soc. Am. B* **9**, 2032–2040 (1992).

Acknowledgements

We thank C. Benko, J. Weitenberg, M. Weidman and L. von der Wense for valuable discussions.

Competing interests

The authors declare no competing interests.

Additional information

Correspondence should be addressed to I.P. or J.Y.